ChemCatChem

ChemCatChem
Chemistry Europe
European Chemical Societies Publishing

RESEARCH ARTICLE OPEN ACCESS

Multifunctional Carbon-Nanotube Supported Catalyst for Efficient Glycerol Hydrogenolysis to 1,2-propanediol

Dominique Lumpp[1] | Samrin Shaikh[1] | Fabian Riebesehl[2] | Charlotte Ruhmlieb[3] | Kai Kruber[4] | Baldur Schroeter[5] | Irina Smirnova[5] | Mirko Skiborowski[4] | Bodo Fiedler[2] | Jakob Albert[1]

[1]Institute of Technical and Macromolecular Chemistry, University of Hamburg, Hamburg, Germany | [2]Institute of Polymers and Composites, Hamburg University of Technology, Hamburg, Germany | [3]Institute of Physical Chemistry, University of Hamburg, Hamburg, Germany | [4]Institute of Process Systems Engineering, Am Schwarzenberg-Campus, University of Technology, Hamburg, Germany | [5]Institute of Thermal Separation Processes, Hamburg University of Technology, Hamburg, Germany

Correspondence: Jakob Albert (jakob.albert@uni-hamburg.de)

Received: 16 November 2025 | **Revised:** 11 February 2026 | **Accepted:** 19 February 2026

Keywords: 1,2-propanediol | carbon nanotubes | glycerol hydrogenolysis | heterogeneous catalysis | structure-activity-selectivity-relationship

ABSTRACT

Multiwall carbon nanotube (NC7000) supported mono-, bi-, and trimetallic catalysts were synthesized and tested in a multi-batch reactor setup supported by data-driven modeling for the chemical hydrogenolysis of glycerol to 1,2-Propanediol (1,2-PDO) at 220°C under 30 bar hydrogen pressure in aqueous solution. ICP-OES, N_2-physisorption, scanning electron microscopy (SEM), transmission electron microscopy (TEM), energy dispersive x-ray spectroscopy (EDX), powder x-ray diffraction (XRD) and x-ray photoelectron spectroscopy (XPS) were used to investigate the physico-chemical properties of the synthesized catalysts. Interesting structure-activity-selectivity correlations could be deduced from the different metal ratios and combinations. While Ru was by far the most active monometallic species ($X = 100\%$), followed by Pt ($X = 80\%$) and Ir ($X = 65\%$), it suffered from a very low 1,2-PDO selectivity ($S < 10\%$). Combining Ru with the more selective transition-metals RuX_2 (X = Fe, Co, or Ni) maintained the high activity ($X > 95\%$) but only moderately increased 1,2-PDO selectivity ($S = 20\%–30\%$). Interestingly, combining Ru with Cu in a bimetallic $RuCu_2$ catalyst slightly decreased activity ($X = 81\%$) but drastically improved 1,2-PDO selectivity ($S = 58\%$). Moreover, a trimetallic combination of $RuMCu_2$ (M = Pt, Pd, Ir) did not further increase activity ($X = 50\%–70\%$) but could push 1,2-PDO selectivity up to 79% for the trimetallic $RuIrCu_2$ catalyst. Most prominently, a final metal ratio variation for the $RuCu_x$ catalyst was derived with the help of the data-driven models producing the most promising $RuCu_3$/NC7000) catalyst combining both high activity ($X = 78\%$) with a very high 1,2-PDO selectivity ($S = 79\%$) resulting in the highest 1,2-PDO yield of 58% in a nearly closed carbon balance ($C > 95\%$). This lays the foundation for implementing this highly active and selective catalyst in a future SMART reactor for glycerol valorization.

1 | Introduction

Due to rising greenhouse gas emissions, the global climate has changed significantly in recent decades, and the effects are also becoming increasingly apparent as extreme weather events occur more frequently [1]. Because of these circumstances and the fact that the production of most platform chemicals is still based on fossil resources, there is a growing interest in the substitution of fossil fuels through green alternatives. Biodiesel synthesis could be a sustainable alternative to fossil diesel production. Biodiesel is a fatty acid methyl ester, which is obtained through the transesterification of fats and oils, where glycerol is obtained as a by-product [2]. Since the production of sustainable glycerol has increased in tandem with the current growth in biodiesel production, its

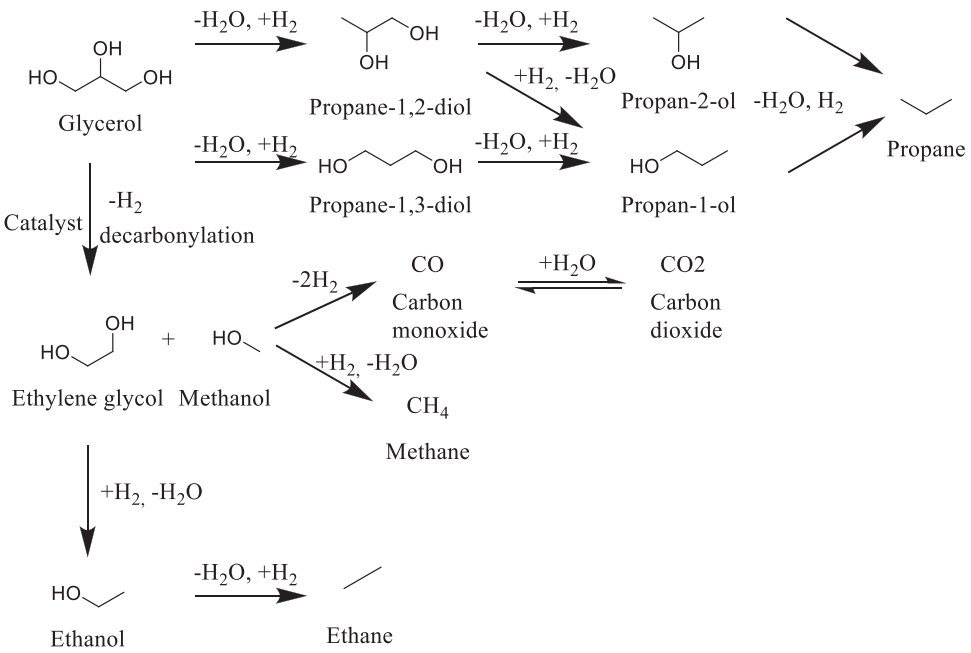

SCHEME 1 | General reaction scheme for the chemical hydrogenolysis of glycerol, based on the mechanistic investigations of Gatti et al. [9].

price has decreased, making it appealing for new applications that it was previously too costly for [3]. One method to utilize the less expensive glycerol is to use it as a platform chemical, to chemically modify it into higher value-added products [4, 5]. One of these higher value products is 1,2-Propanediol (1,2-PDO), which can be obtained by the hydrogenolysis of glycerol. 1,2-PDO is used as a monomer for the polymer industry, pharmaceuticals, cosmetics, food, and animal feed industry [6, 7].

Glycerol goes through selective hydrogenolysis to produce 1,2-PDO in a two-step chemical process (Scheme 1). In the first step, glycerol undergoes acid-catalyzed dehydration to produce the intermediate Prop-2-en-1,2-diol, followed by a keto-enol-tautomeric rearrangement to produce acetol. In the second step, acetol is selectively hydrogenated to 1,2-PDO [8]. The biggest challenge is to develop a catalyst that avoids the formation of C2 and C1 products like ethylene glycol or methanol through C—C bond cleavage but favors initial dehydration. At the same time, the dehydration needs to take place at the primary hydroxy group in order to avoid the parallel reaction leading to 1,3-PDO formation [9]. The dehydration of the secondary hydroxy group is kinetically controlled, while the reaction via the primary hydroxy group is thermodynamically preferred [10]. Moreover, the subsequent hydrogenolysis resulting in the formation of monohydroxy alcohols needs to be inhibited, presenting a challenging optimization issue for the development of an efficient catalyst [6, 11]. Several heterogeneous catalysts based on noble metals like Pt, Pd, Ru, Rh, and Re or transition metals like Cu, Ni, Co, Fe, or Zn have been used for the hydrogenolysis of glycerol [11, 12]. Noble metals provide a high activity toward glycerol conversion, especially in the hydrogenation step. However, their ability to perform C—C bond cleavage leads to a lower selectivity. Wang et al. tested different noble metals, like Pt, Pd, Ru, and Rh, supported on monoclinic ZrO_2, where Ru showed the highest activity [13]. This could be confirmed by other studies, as long as the Ru has acidic species [12, 13]. Nonacidic Ru mainly forms undesired short-chain alkenes via thermal-induced formation of acrolein, which is followed by decomposition to CO [14–16]. Conversely, transition metals possess high selectivity toward 1,2-PDO, but lack activity compared to noble metals. Within the group of transition metal-based catalysts, Cu catalysts have been the ones most widely used for the production of 1,2-PDO, both in liquid and vapor phase [17]. Cu supported on different materials like TiO_2, Al_2O_3, MgO, and SiO_2 showed promising results [18–21]. Ni was also found to be a promising candidate for glycerol hydrogenolysis, which can be immobilized on various supports like SiO_2, C, and Al_2O_3, despite not being as widely used as Cu [7, 22, 23]. Co hasn't been used that frequently for the reaction because of its low intrinsic activity [10]. Fe is also discussed as a promising candidate for the reaction because of its low cost and low environmental footprint. For example, Soares et al. reported the use of Fe to dope the Pt/Al_2O_3 catalyst. The Pt-Fe interactions generated new active sites for glycerol hydrogenolysis [24].

This approach of combining two different metal species on a support material is a widely known technique in catalyst development. In the case of glycerol hydrogenolysis, the idea is to combine the activity of noble metals with the selectivity of transition metals. For the role of the noble metal, Ru seems to be well suited, as the acidic Ru sites help in catalyzing the first protonation step [25]. In the literature, several such bimetallic catalysts have been reported. For example, Li et al. used a carbon nanotube-supported RuFe bimetallic catalyst, where they were able to achieve complete conversion with a selectivity up to 75% [26]. The high catalyst activity was explained by the synergetic effects between RuFe bimetallic nanoparticles and the interaction of these nanoparticles and Fe oxides on a carbon nanotube (CNT) support. By using Cu-Ru NPs supported on CNTs, Wu et al. were able to find out that in their catalyst system, tiny Ru clusters didn't perform in the hydrogenolysis of glycerol, but instead activated and generated hydrogen by glycerol reforming [17]. This activated hydrogen was transferred to the Cu surface nearby via hydrogen

spillover, therefore increasing catalyst activity compared to the pure Cu catalyst. Liu et al. synthesized RuCu bimetallic catalysts supported on different supports like SiO_2, TiO_2, Al_2O_3, and ZrO_2 and tested them under harsh reaction conditions of 100 bar H_2 pressure. Supporting the nanoparticles on ZrO_2 gave the best results with full glycerol conversion and a selectivity of 78% [27]. Moreover, Sherbi et al. were able to add Cu to Ru nanoparticles dispersed on a commercial CNT support via an improved wetness impregnation method [28]. This significantly enhanced the reducibility and modified the surface of the resulting Ru-Cu species. The resulting bimetallic Ru-Cu/CNT catalyst, as well as the surface interaction between Cu and Ru, led to a promoting effect resulting in a preference for C—O bond cleavage promoted by Cu over C—C bond cleavage catalyzed by small Ru nanoparticles. By employing this catalyst for the hydrogenolysis of glycerol, a superior 1,2-PDO selectivity of 93.4% was achieved [29].

The aim of this study was to verify the most important structure-activity-selectivity correlations for the production of 1,2-PDO by systematically synthesizing various mono-, bi-, and trimetallic CNT-supported catalysts. With the help of a rigorous predictive data modeling approach, the optimal ratio between Ru and the most promising second metal was selected and verified by experimental testing.

2 | Results and Discussions

2.1 | Catalyst Characterization

The carbon nanotubes that were used as a support for all catalysts synthesized in this study were commercially available multi-walled CNT NC7000 by Nanocyl SA., Belgium, which is a nanoparticle powder widely applied in industrial-scale CNT-modified materials (Table S2). First, a series of various mono-, bi-, and trimetallic catalysts supported on NC7000 was synthesized based on an established wetness impregnation method described in the Materials and Methods section. Table S1 shows a compilation of all synthesized mono-, bi-, and trimetallic catalysts used in this work. The desired metal ratios and metal loadings could be achieved by the applied synthesis method for all synthesized compounds.

Table 1 summarizes the textural properties of the synthesized bi- and trimetallic catalysts. The corresponding data for the monometallic ones are shown in Table S3. In general, the catalysts exhibit a type IVa isotherm, as expected for mesoporous materials. Compared to pure CNTs, the total surface area decreases after metal impregnation. This decrease can be attributed to metal particles either being deposited within the pores or blocking their entrances. However, the total pore volume increased upon metal loading, suggesting that the metals were primarily deposited on the outer surface of the CNTs, possibly near the pore openings. This could lead to an extension of the accessible pore system, thereby increasing its volume. If the metals were deposited deep within the pore channels, a decrease in pore volume would be expected. Additionally, the average pore diameter was found to be slightly larger in the bimetallic catalysts compared to pure CNTs. This may indicate that smaller pores are more likely to be blocked by metal particles, rendering them inaccessible and shifting the average diameter toward larger values. In contrast, wider pores are less likely to be completely blocked, which helps explain the observed increase in pore volume. No significant changes in the range of pore sizes and overall mesopore volume, $0.97 \pm 0.10\ cm^3/g$ on average, were observed due to metal loading, as seen in the pore size distributions, shown in Figures S2 and S3. The slight decrease in specific surface area of loaded samples as compared to the pristine reference might be attributed to (a) the additional weight of metallic components and (b) to blockage of some smaller mesopores, as indicated in a slight loss of mesopore volume in the range of pores <9 nm in the case of bi- and trimetallic catalysts.

The x-ray photoelectron spectroscopy (XPS) results of the monometallic Ru (Figure S7) and Cu (Figure S8), as well as the bimetallic $RuCu_2$ catalyst is shown in Figure 1. The spectra prove that Ru is in its metallic state, indicated by the Ru3d5/2 peaks with a binding energy of 280.4 eV for the monometallic Ru as well as for the bimetallic catalyst, respectively. It was observed that adding transition metals to the monometallic Ru catalyst doesn't influence the oxidation state of Ru. Looking at the oxidation state of Cu, the Cu2p at 932.4 eV corresponds to Cu in its metallic state. The Auger peaks of the Cu at 570.3 eV confirmed that Cu has an oxidation state of +2 [30]. This indicates that Cu is present in both oxidation states in the bimetallic catalyst. As confirmed by the TPR results (Figure 4), the temperature program exhibited the reduction of both metals. However, post-reduction, air exposure of Cu could be responsible for its partial oxidation, which could impact the performance of the catalyst negatively, as metallic Cu is the catalytically active species. Ru, as a noble metal, is less reactive with air, so its oxidation state is more stable. Interestingly, for the monometallic Cu/NC7000 catalyst (Figure S8), it was observed that the ratio of Cu (+2) decreased in comparison to the bimetallic Ru-Cu catalyst. This indicates that the presence of Ru promotes Cu oxidation. For the $RuFe_2$/NC7000 catalyst, the 2p3/2 signal at 710.8 eV, shown in Figure S4, is a strong indicator that the Fe in the catalysts is present in its oxidized form (+3). Unlike the Cu system, there is no indication of elemental Fe present, showing that the Fe particles are less stable under atmospheric conditions during their short exposure. The bimetallic Co and Ni catalysts exhibited Ru in its elemental form, while the corresponding transition metal was present in its oxidized form, as shown in the spectra in Figures S5 and S6, respectively.

Morphological analysis of the bimetallic catalysts with transmission electron microscopy (TEM) and energy dispersive x-ray (EDX) mapping is shown in Figures 2, S10, and S11. The EDX mapping of the bimetallic $RuCu_2$ catalyst showed that Ru and Cu were well dispersed over the surface of the CNTs. This was confirmed by a very high dispersion of 72.5%. The particle size distribution showed that the metal particles were the smallest compared to the other bimetallic catalysts. This resulted in a better surface-to-volume ratio, leading to more active sites on the surface. Moreover, it was observed that after reduction, the particle size increased. This may be due to the sintering of the metals or the increased radius of the elements compared to their ions, which could be an indicator of a change in the oxidation state. The same was observed for the bimetallic $RuFe_2$ catalyst. In the bimetallic $RuCo_2$ catalyst, it was observed that the Co was agglomerated at the surface. This can be explained through Co impurities, which were found in the pure CNTs (Table S2), as Co is

TABLE 1 | Physico-chemical properties of the used catalysts.

Catalyst/support	[a]Total surface area(m^2g^{-1})	[b]Pore volume(cc/g)	[b]Pore diameter(nm)	[c]Metal dispersion(%)	[c]Particle diameter(nm)	[c]Particle diameter after reduction/nm
NC7000	252	0.919	14.8	—	—	—
$RuCu_2$/NC7000	205 ± 2	1.155	22.6	72.50	1.14 ± 0.21	1.83 ± 0.43
$RuFe_2$/NC7000	193 ± 1	0.924	19.3	66.00	1.50 ± 0.39	2.01 ± 0.89
$RuCo_2$/NC7000	197 ± 2	1.039	21.3	18.70	1.73 ± 0.23	7.08 ± 0.40
$RuNi_2$/NC7000	209 ± 2	1.042	20.1	50.50	1.25 ± 0.26	2.63 ± 0.67
$RuIrCu_2$/NC7000	209 ± 2	0.946	18.4	35.40	3.74 ± 5.29	—
$RuPdCu_2$/NC7000	200 ± 2	0.899	18.2	46.60	2.85 ± 1.29	—
$RuPtCu_2$/NC7000	175 ± 1	0.832	19.2	30.25	4.39 ± 3.04	—-

[a]Determined with N_2-physisorption using the BET method,
[b]Determined with N_2-physisorption using the BJH method,
[c]Determined with HR-TEM [26].

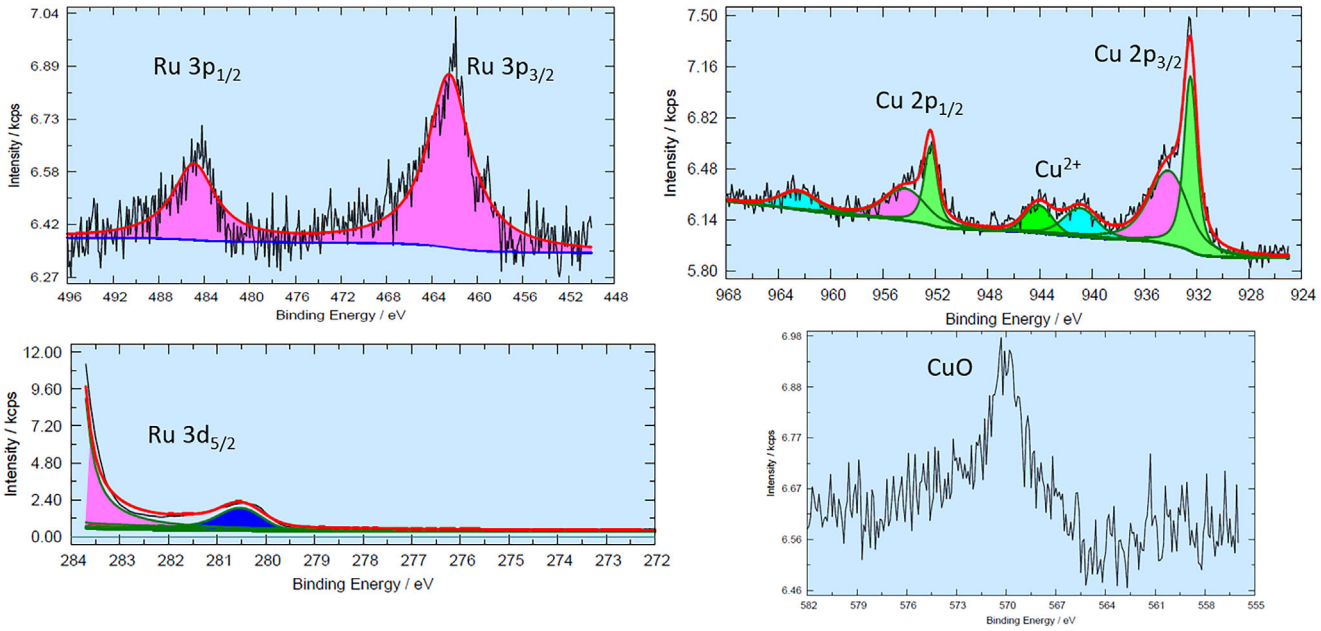

FIGURE 1 | XPS spectra of the bimetallic $RuCu_2$/CNT catalyst. (a) Ru 3p, (b) Cu 2p, (c) Ru 3d5 region, (d) zoom on 3d5 signal of Ru.

one of the typical metals used in CNT production. The bimetallic $RuNi_2$ catalyst showed in its EDX map large Ru chunks, resulting from agglomeration, as in the other metal combinations. Taking a look at the EDX-mapping of the trimetallic catalysts shown in Figure S12, it could be observed that Ru, Cu, and Pd are nicely distributed at the surface of the CNT; little agglomerations of Pd could be seen. The Pt-containing catalyst shows agglomerated particles of all three elements. This could be due to the effect that ethanol was used in the synthesis as a solvent due to the different solubility of the precursor used. In contrast, a nice distribution could be observed for all three elements for the $RuIrCu_2$ catalyst.

The high-resolution transmission electron microscopy pictures (HR-TEM), shown in Figure 3, indicate that after the catalyst synthesis, the structure of the CNTs remained intact, as the multiwalled structure showed no changes compared to the pure CNTs shown in Figure S9. It was also observed that the metal particles were distributed at the surface of the CNTs. The presence of these active sites is desirable, as they are more accessible for the glycerol molecules. As this was observed for all the synthesized catalysts, the impregnation method provided similar results when using different metals. After the reduction of the catalysts in the tube furnace observed for the bimetallic $RuCu_2$, $RuFe_2$, and $RuNi_2$, no changes in the HR-TEM images were observed, confirming that no structural changes in the CNTs or sintering of the metal particles were observed. However, the $RuCo_2$ catalyst exhibited a damaged CNT structure.

The catalysts were further analyzed by powder x-ray diffraction (PXRD), the diffractograms are shown in Figures S13 and S14. The pure CNT support showed the two broad characteristic peaks at 26° and 43° that can be assigned to the graphitic carbon in the CNT. Whereas, in the case of the monometallic Ru/CNT catalyst, no characteristic reflexes of Ru were observed, even

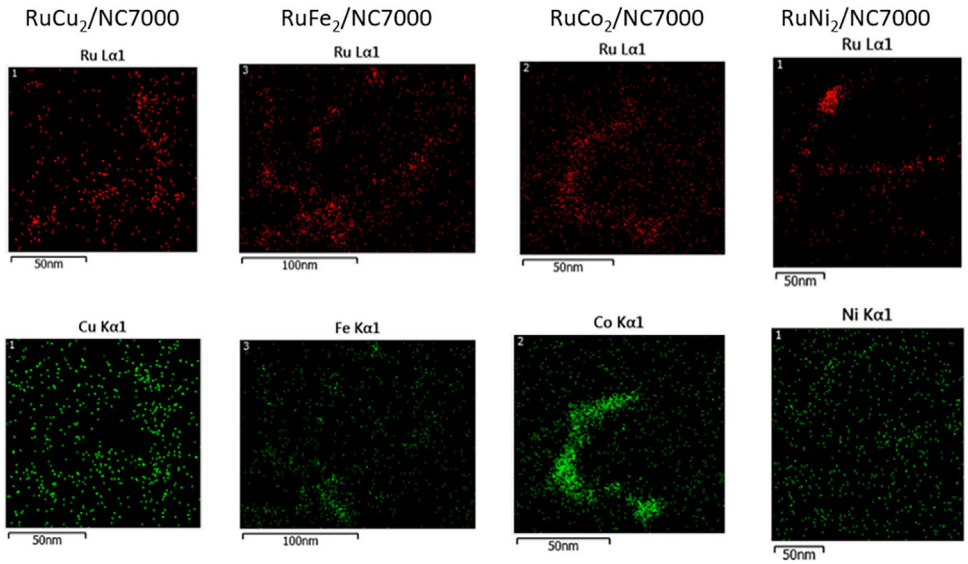

FIGURE 2 | TEM-EDX mapping of the bimetallic catalysts.

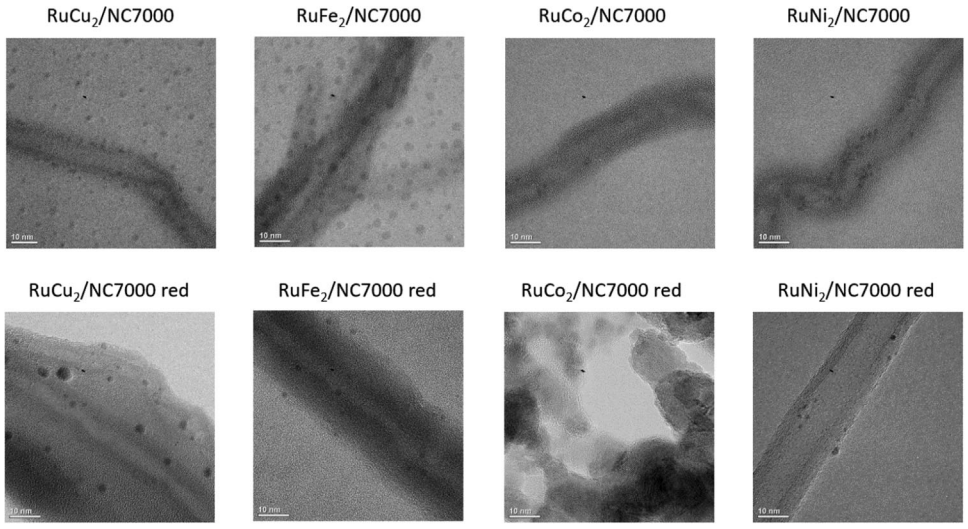

FIGURE 3 | HR-TEM of the bimetallic catalysts before (top line) and after (bottom line) the reduction.

though the presence of Ru in this catalyst was confirmed by ICP-OES and TEM-EDX mapping. This may be because the Ru particles in the catalyst are very small or well dispersed, which cannot be observed in the diffractogram, as they get overlaid by the amorphous signal of the CNT. The same goes for Ru in every bi- and trimetallic catalyst. The Fe/CNT catalyst, it showed a reflection at 33°, which isn't present in the bimetallic catalyst. By adding another metal while keeping the overall loading constant, the intensity of the reflex decreased and was overlaid by the noise of the CNTs, as seen in Figure S14.

Figure 4 represents the results of the H_2-temperature programmed reduction (H_2-TPR) for the bimetallic catalysts. For the $RuCu_2$/CNT catalyst, the reduction peaks of Ru (+3) and Cu (2+) to its metallic state have been merged together in a wide peak between 300 and 550°C. The additional peak at around 800°C can be assigned to the formation of methane from the CNTs, which is catalyzed by the Ru metal in the catalyst [31]. For the $RuFe_2$/CNT catalyst, the Ru reduction peak was merged with the reduction of Fe (+3) to Fe (+2). The shoulder that can be observed is assigned to the reduction of Fe (+2) to Fe (0) (Figure S15). Compared to the literature, the Ru reduction temperature is increased, due to the higher Fe ratio (Figure S15) [22]. The decomposition to methane can be observed at a lower temperature. This behavior can also be observed for the Co and Ni containing catalysts (Figure S15). It seems that those catalysts have not only a higher activity in the valorization of glycerol, but also in the decomposition of the CNTs. For the Co-containing catalyst, this can explain the partial decomposition of the CNTs as observed in the HR-TEM images. Comparing the TPRs of the trimetallic catalysts with the $RuCu_2$/CNT catalyst (Figure S17), it was observed that the reduction maximum was slightly decreased. It indicates that the addition of an additional noble metal increases the reducibility toward lower temperatures, as the H_2 is adsorbed on the surface

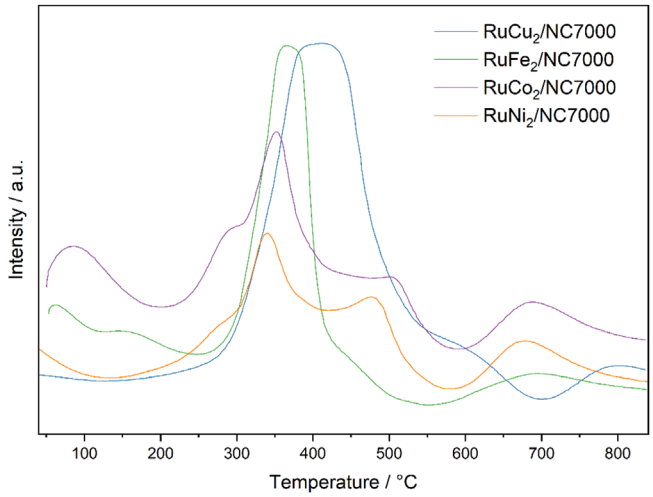

FIGURE 4 | H_2-TPR of the bimetallic catalysts.

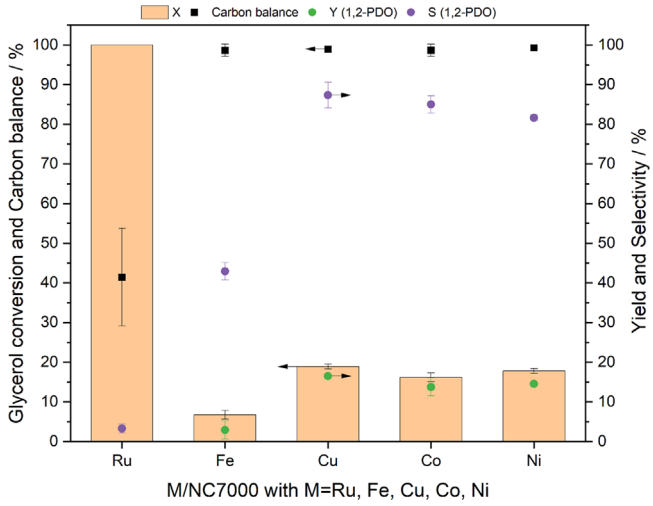

FIGURE 5 | Catalytic performance of monometallic Ru, Fe, Cu, Co, and Ni supported on CNT catalysts. m_{Cat} = 200 mg, metal loading = 5 wt.%, T = 220°C, p_{H2} = 30 bar, t = 20 h, n = 1000 rpm, c(Gly) = 20 wt.%, 10 g reaction mixture.

more easily [32]. In addition, the peak of the Pd- and Pt-based trimetallic catalysts seems to be broadened in comparison to the $RuCu_2$/CNT (Figure S16), suggesting that there are more metallic sites on the surface that are being reduced, leading to a higher hydrogen consumption.

2.2 | Catalytic Hydrogenolysis Experiments

Control experiments without a catalyst showed that only negligible glycerol conversion occurs by pure thermal activation (<1%). The pure NC7000 shows a very low blind activity of 3.7%, which might be caused by metallic impurities like Al and Fe stemming from the CNT synthesis (Table S5). The results of the glycerol hydrogenolysis experiments for the monometallic catalysts containing Ru, Fe, Cu, Co, or Ni as active species supported on NC7000 are shown in Figure 5.

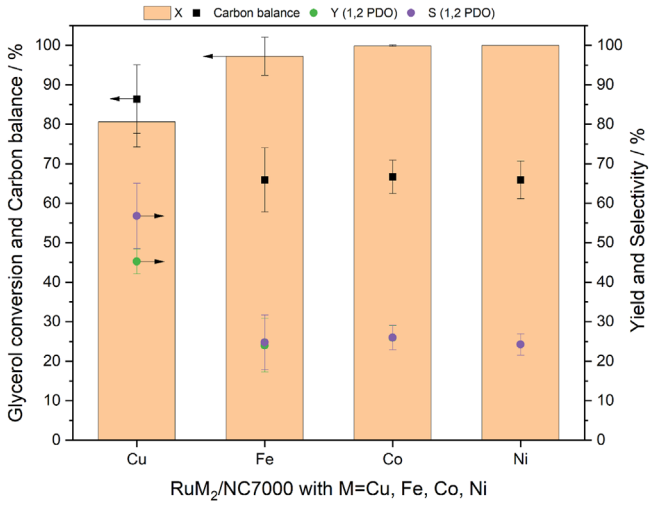

FIGURE 6 | Catalytic performance of the bimetallic RuM_2 catalysts with M = Cu, Fe, Co, and Ni supported on CNT. m_{Cat} = 200 mg, metal loading = 5 wt.%, T = 220°C, p_{H2} = 30 bar, t = 20 h, n = 1000 rpm, c(Gly) = 20 wt.%, 10 g reaction mixture.

The Ru catalyst showed complete glycerol conversion. However, as Ru also exhibits excessive C—C-bond cleavage [14], the catalytic experiment resulted in a very low yield for the desired 1,2-PDO of only 4%, while a high yield of undesired methane was formed, which is the reason for the low carbon balance in this experiment. The transition metal catalysts are a lot less active with glycerol conversions around 20% after 20 h reaction time. At the same time, they showed a way higher selectivity toward the desired 1,2-PDO between 45% (Fe) up to 88% (Cu). As those metals cannot perform C—C-bond cleavage, only the dehydration route of the reaction network can take place (compare Scheme 1), showing their clear preference for C—O bond cleavage. Because of their low activity, those catalysts were not able to perform the follow-up hydrogenolysis of 1,2-PDO to iso or n-propanol under the applied reaction conditions of 220°C and 30 bar H_2 pressure. While the monometallic Cu, Co, and Ni catalysts have a similar conversion of glycerol of about 20%, the Cu catalyst possessed the highest selectivity, resulting in the highest overall 1,2-PDO yield in this series (Y = 19%), making it the most promising of the tested transition metals. The lower activity of the Fe-based catalyst can be explained by its low stability, as the Fe gets oxidized during the reaction.

In the next step, a strategy to combine the activity of Ru with the selectivity of the transition metals was implemented. A ratio of 1:2 based on the previous study by Sherbi et al. was chosen for all bimetallic catalysts tested [28]. The results are shown in Figure 6. Reproducibility studies (Figure S22) confirmed the standard deviation for the conversion of 1.09%, 2.29% for the 1,2-PDO yield, and 2.18% for the 1,2-PDO selectivity, as well as 1.56% for the carbon balance. The combination of Ru with another transition metal improved the overall yield for all bimetallic catalysts. Full conversion was achieved by the bimetallic catalysts containing Ru and Fe, Ni or Co, while the bimetallic RuCu catalyst showed a glycerol conversion of 85%. Despite being the least active catalyst, the RuCu catalyst attained the highest yield of 1,2-PDO, exceeding 40%. This result is due to Cu enhanced selectivity consistent with the previous studies [28]. In contrast,

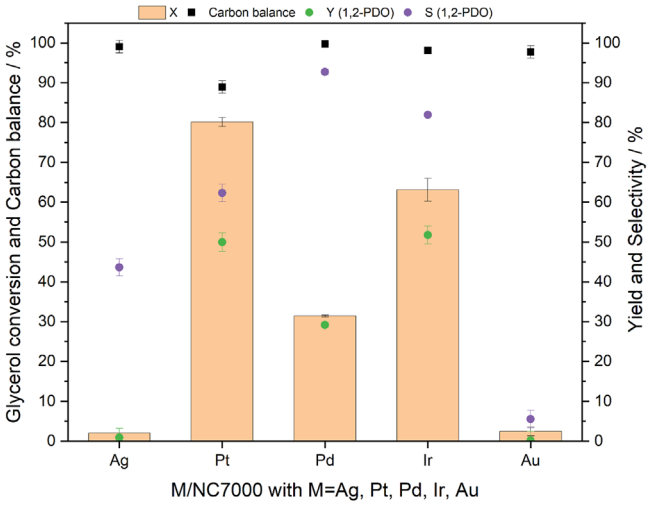

FIGURE 7 | Catalytic performance of Ag, Pt, Pd, Ir, and Au supported on CNT. m_{Cat} = 200 mg, loading = 5 wt.%, T = 220°C, p_{H2} = 30 bar, t = 20 h, n = 1000 rpm, c(Gly) = 20 wt.%, 10 g reaction mixture.

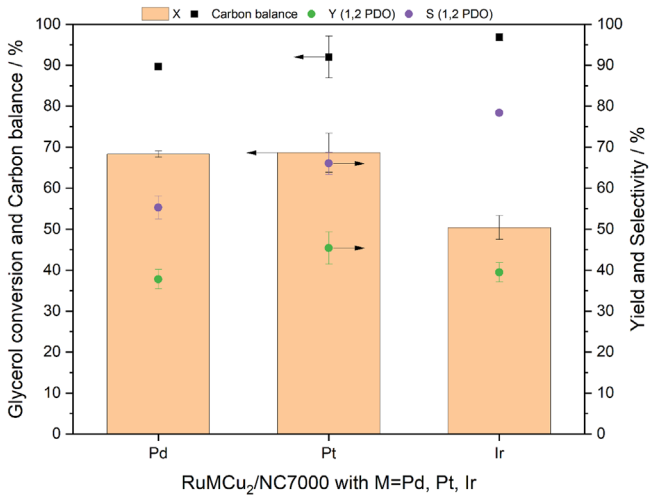

FIGURE 8 | Catalytic performance of the trimetallic $RuCu_2M$ catalysts supported on CNT, with M = Pd, Pt and Ir. m_{Cat} = 200 mg, metal loading = 5 wt.%, T = 220°C, p_{H2} = 30 bar, t = 20 h, n = 1000 rpm, c(Gly) = 20 wt.%, 10 g reaction mixture.

the bimetallic catalysts containing Fe, Ni, and Co exhibited comparable lower 1,2-PD selectivities to the Cu system between 60%–75%. In comparison to the other bimetallic systems, the $RuCu_2$/NC7000 catalyst has the highest pore volume, implying a good accessibility of the active sites and higher diffusion rates compared to the catalysts with a smaller pore volume. The high surface area leads to more active sites that are accessible for the adsorption of glycerol molecules. At the same time, the catalyst has the smallest particle diameter of the investigated systems, which is an indicator for well-dispersed metal particles and a good surface-to-volume ratio. Besides the inferior structural properties of the Fe, Co, and Ni systems, other parameters could also be responsible for their worse performance compared to the Cu system. The TEM-EDX pictures of Ni/NC7000 in Figure 2 show that the Ru particles are slightly agglomerated compared to the other catalysts. For the Co/NC7000 catalyst, the damaged structure of the CNTs after reduction could have a major impact on the catalyst activity. This effect may also be responsible for the rise in particle size compared to before the reduction. Those bigger metal particles have a lower surface-to-volume ratio, resulting in a worse utilization of the active metals. As seen in the XPS-measurements in Figures 1 and S4–S8, the transition metal in the observed systems is susceptible to oxidation when exposed to air during the reaction procedure, which can negatively influence the catalytic activity.

In the next step, it was investigated if doping the bimetallic $RuCu_2$ catalyst with a noble metal improves the catalytic performance even further by enhanced hydrogen adsorption and spillover, as suggested by literature [17, 24]. Therefore, several monometallic noble metal catalysts were synthesized and tested for the glycerol hydrogenolysis (Figure 7). While the Ag and Au-based catalysts showed only very low conversion of glycerol <5%, the other three catalysts containing Pt, Pd, and Ir appeared to be promising with conversions between 35%–80%. This can be explained by the low metal loading for Ag, as it can be deduced from the ICP results in Table S1, and the low reactivity for Au-based catalysts in this reaction system, as Au is usually used as a promoter in the catalytic conversion of glycerol to 1,3-propanediole [31]. The Pt-containing catalyst has the highest activity with a glycerol conversion of 80%, while the Pd one has a high 1,2-PDO-selectivity of >90%. Despite the fact that the Ir-based catalyst (S = 82%) is not as selective as the Pd catalyst or as active as the Pt-based catalyst, it produced the highest overall 1,2-PDO yield of 52%.

As a result of these experiments, trimetallic catalysts containing Ru, Cu, and one of the noble metals (M = Pt, Pd, Ir) were synthesized and tested. The results of the catalytic experiments with these trimetallic catalysts are shown in Figure 8. The maximum achieved 1,2-PDO yields were 48.6% ($RuPtCu_2$NC7000), 40.2% ($RuIrCu_2$/NC7000), and 38.8% ($RuPdCu_2$/NC7000), respectively. The reason is probably the resulting lower Ru loading in those systems, as the total metal loading was kept constant at 5 wt% to guarantee comparability. Therefore, by keeping the overall metal loading constant, the Ru ratio in the trimetallic catalysts was lower than in the bimetallic catalysts. As a result, the catalyst loses activity compared to the bimetallic ones. The same can be observed for the Cu ratio in trimetallic catalysts, as reducing Cu levels by introducing a third, less selective metal results in decreased overall selectivity to 1,2-PDO (79% for $RuIrCu_2$/NC7000).

Building on the experimental results, simplified polynomial models were implemented in MATLAB, making use of the Statistics and Machine Learning toolbox to analyze the data and deduce statistical correlations for further catalyst improvement (Table S6). Moreover, strategies were derived for further improving 1,2-PDO selectivity and glycerol conversion. Details can be found in the Data Modeling Section of the Supporting Information. As indicated by the model statistics in Table S6, the models accurately describe the experimental data with statistically significant parameters (adjusted R^2 = 0.953 for conversion, 0.985 for selectivity). To assess generalization, the models were validated against 12 held-out experiments not used for fitting, yielding validation R^2 values of 0.813 for conversion and 0.939 for selectivity (Figure 9). The models further highlight the parabolic shape of the achievable 1,2-PDO yields that supports the improvement by

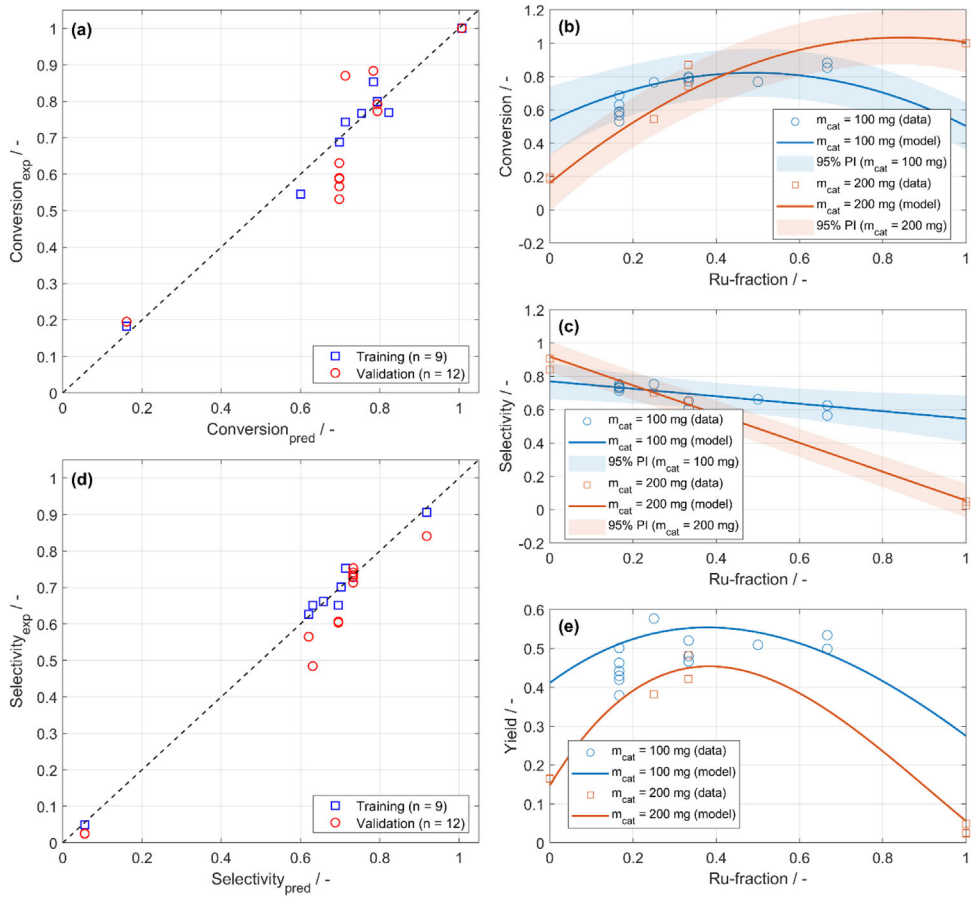

FIGURE 9 | Parity plots for conversion (a) and selectivity (d) comparing training and validation data, alongside model predictions of conversion (b), selectivity (c), and yield (e) as a function of Ru-fraction for the bimetallic RuCu catalyst. Shaded regions indicate 95% prediction intervals.

the bimetallic catalyst and the improvements for the catalyst mass of 100 mg.

Figure 9 shows an illustration of the parity plots and predicted 1,2-PDO selectivity as well as glycerol conversion and resulting 1,2-PDO yields.

As highlighted by the model statistics in Table S7 and the parity plots in Figure 9, the models accurately represent the experimental data with statistically significant parameters. While they provide valuable insights, the small and sparse experimental dataset, combined with missing measurements in certain regions of the design space, limits their predictive reliability, particularly near pure precursor compositions at low catalyst mass. Nevertheless, the models demonstrate robust generalization when evaluated on 12 held-out experiments not used for fitting (Figure 9a,d). To further improve data coverage and enable surrogate-based optimization strategies such as Bayesian optimization, a follow-up experimental campaign guided by statistical design of experiments (DoE) is recommended to systematically explore undersampled regions of the design space.

In addition to the validated RuCu model, an extended polynomial model was fitted to the full set of 16 mono-, bi-, and trimetallic experiments spanning all five metals (Ru, Cu, Pt, Pd, Ir) to explore the broader design space (Table S7). Given the small dataset relative to the number of features, these predictions should be interpreted with caution (Figure S23). Optimization of the extended model in the confined design spaces indicated that the highest yield was obtained for the bimetallic RuCu catalyst, while the trimetallic $RuPtCu_2$ catalyst also provides potential for competitive or superior results, considering a ratio of 1:2:1, instead of the experimentally investigated 1:1:2 ratio, as illustrated in Figure 8. Furthermore, the model predicts 1,2-PDO yields above 50% for other bimetallic combinations such as RuPt and PtCu, which remain to be validated experimentally in future studies.

In the final step of the catalyst development, the ratio between the two most promising components, Ru and Cu, as suggested by statistical data modeling, was varied. The catalytic results are shown in Figure 10. The outcome aligns well with the earlier findings. As expected, the catalyst with the highest Ru ratio, Ru_2Cu, achieved the highest glycerol conversion of 86%, due to the high activity of Ru. Due to its high activity, this catalyst underwent more side reactions and exhibited the lowest 1,2-PDO selectivity of only 60%. With increasing Cu content, the 1,2-PDO selectivity was drastically improved up to 80%; however, the activity of the catalyst was found to decrease with increasing Cu content. This resulted in a maximum 1,2-PDO yield of 58% at the ratio of $Ru:Cu_3$ of 1:3. With this catalyst, we performed a recycling study, where the catalyst was separated from the reaction solution by centrifugation and reduced again in the reduction oven, to

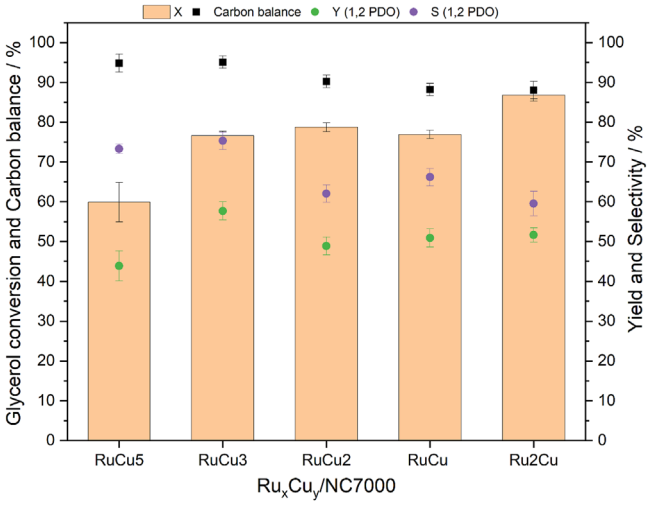

FIGURE 10 | Catalytic performance of the bimetallic catalyst with different RuCu ratios supported on CNTs. m_{Cat} = 100 mg, loading = 5 wt.%, T = 220°C, p_{H2} = 30 bar, t = 20 h, n = 1000 rpm, c(Gly) = 20 wt.%, 10 g reaction mixture.

counteract the oxidation of Cu during air exposure. The results are shown in Figure S24. However, a drop in conversion to 33% for the first recycle step, resulting in a 1,2-PDO yield of 28%, was observed. This drop in performance might be attributed to particle agglomeration, as already discussed in the literature [12].

3 | Materials and Methods

3.1 | Chemicals

The glycerol used for the experiments was purchased from Alfa Aesar with a purity of 99+% and used without further purification. The used NC7000 CNTs were purchased from Nanocyl. For the catalyst synthesis, the following metal precursors were used: $RuCl_3$*$3H_2O$ (Sigma–Aldrich, 38%–42% Ru), Cu(II)$(NO_3)_2$*$3H_2O$ (Sigma–Aldrich, 99%), Fe $(NO_3)_3$*$9H_2O$ (Merck, 98%), $CoCl_2$ anhydrous (Sigma–Aldrich, 98%), $NiCl_2$ (Sigma–Aldrich, 98%, $AgNO_3$ (Roth, 99.9%), Palladium(II)acetate (VWR, 98%), Platinum(II) acetylacetonate (98% from ABCR), Hydrogen hexachloroiridate(IV) hydrate (Sigma Aldrich, 36%–44% Ir), Tetrachloroauric(III) acid trihydrate from (VWR, 99.99%).

3.2 | Catalyst Preparation

The powder catalyst was synthesized using an improved procedure reported by Sherbi et al., [28]. via wetness impregnation. In a usual synthesis for a 2 g batch of catalyst, 1.9 g of the Nanocyl NC7000 was added to a round-bottom flask. The metal precursors were dissolved in 200 mL of water, except for the Pt-based catalysts, where ethanol was used as a solvent, and the precursor solution was added one after another in the round-bottom flask. The catalyst solution was heated to 80°C and stirred at 110 rpm using a rotary evaporator for 5 h. After that, the liquid was removed. The catalyst was mortared carefully and dried in an oven (Nabertherm L9/11) for 8 h at 110°C.

3.3 | Reaction Procedure

Before the reaction, the catalyst was reduced in a tube furnace (Nabertherm R50/250/12) using forming gas with 5 vol% H_2 in N_2 at 550°C for 8 h with a heating rate of 120°C/h and a gas flow of 50 L/h.

The hydrogenolysis reactions were carried out in a 4-fold multi-batch reactor setup using high-pressure stainless-steel reactors (material number: 1.4571) with a reaction volume of 21 mL (Figure S1). Normally, 200 mg of catalyst was used, unless otherwise specified. In addition to the catalyst, 10 g of a substrate solution consisting of 20 wt-% glycerol and demineralized water was added to the reactor, as well as a PFTE stirring bar. The reactors were closed and placed on the heating blocks made of aluminum on a stirring plate and connected to rupture discs and the gas inlet. The stirrer was set to 300 rpm, and the reactors were then flushed three times with N_2, and a pressure of 30 bar was built up for the pressure test. If the pressure remained constant for over one hour, the pressure was released. The reactors were then flushed twice with H_2 and then pressurized to approximately 30 bar, so the pressure reached a value of approximately 50 bar at the desired reaction temperature. After the reaction temperature was reached, the stirrer speed was set to 1000 rpm to start the gas entrainment. After a typical reaction time of 20 h, the reaction was stopped by switching off the heat supply, and the reactors were cooled down to room temperature. After the reactors reached room temperature, gas samples were taken from the reactor using gas bags and analyzed by GC. The catalyst was separated by filtration. The liquid phase was then analyzed via HPLC and ^1H and ^{13}C NMR spectra to confirm the identity of the products.

3.4 | Calculations

The glycerol conversion was calculated according to Equation (1).

$$X = \frac{c_{0,\,Glycerol} - c_{Glycerol}}{c_{0,\,Glycerol}} \times 100\% \quad (1)$$

The yields of both liquid and gas-phase products were calculated by Equation (2).

$$Y_i = \frac{c_i}{c_{0,\,Glycerol}} \times 100\% \quad (2)$$

The selectivity to the desired product 1,2-PD was calculated by Equation (3).

$$S_i = \frac{Y_i}{X} \times 100\% \quad (3)$$

In order to fully reveal the reaction mechanism, the carbon balance for each experiment was calculated by Equation (4).

$$Carbon\ balance = \frac{\sum n_i \times number\ of\ carbons}{n_{Glycerol} \times 3} \times 100\% \quad (4)$$

The productivity of the catalysts as an evaluation, shown in Table S9, criteria was determined using Equation (5).

$$P_{cat} = \frac{m_{1,2-PDO}}{m_{acive\ metal} * t_R} \quad (5)$$

3.5 | Analytics for Catalyst Characterization

3.5.1 | Inductively Coupled Plasma Optical Emission Spectroscopy (ICP-OES)

The sample preparation is described in the Supporting Information. The elemental concentrations of the following elements were determined by inductively coupled plasma optical emission spectrometer (ICP-OES, Perkin Elmer, Avio 550): Al (analytical wavelength: 396.153 nm), Fe (238.204 nm), Cu (327.393), Co (228.616 nm), Ru (240.272), Pd (340.458), Pt (265.945) and Ir (205.222). To check for reproducibility and accuracy, individual sample splits were measured three times and checked against quality control standards with known certified concentrations. The concentrations of the samples were determined via external calibration against standards with known concentrations. Blanks were usually negligible but were subtracted from the individual sample element concentrations if significant. The quality control standards were usually between 90% and 110%. If significant outliers were detected, measurements were repeated.

3.5.2 | X-Ray Photoelectron Spectroscopy (XPS)

The XPS measurements were performed on an ESCALAB 220iXL (ThermoFischer Scientific) with monochromated Al Kα radiation ($E = 1486.6$ eV). Samples are prepared on a stainless-steel holder with conductive double-sided adhesive carbon tape. The electron binding energies were obtained without charge compensation and referenced to the C 1s peak, assuming sp^2 carbon as the main component at 284 eV. For quantitative analysis, the peaks were deconvoluted with Gaussian–Lorentzian curves using the software Unifit 2023, the peak areas were divided by the transmission function of the spectrometer, and the element-specific sensitivity factor of Scofield.

3.5.3 | Powder X-Ray Diffraction (PXRD)

Crystal structure determination was performed through powder x-ray diffraction (p-XRD) using a Panalytical MDP X'Pert Pro diffractometer, operating in Bragg–Brentano geometry with Cu Kα radiation ($\lambda = 0.1541$ nm). The diffraction angle was measured over a range of 5 to 90°, with a sampling rate of 0.013° and a time per step of 72.42 ms.

3.5.4 | Scanning Electron Microscope (SEM) and Energy Dispersive X-Ray (EDX)

SEM imaging with various magnifications was done at 5 kV acceleration voltage using a LEO Gemini 1550 (Zeiss) equipped with an Inlens detector and an ESB detector. The EDX data was recorded within the same setup at 20 kV using the EDX detector Ultim Max 100 (Oxford Instruments). An integration time of 80 s was set for all EDX measurements on several areas of each sample, respectively. The software AzTec (Oxford Instruments) was used for data evaluation.

3.5.5 | High Resolution Transmission Electron Microscopy (HRTEM) and Energy Dispersive X-Ray (EDX) Mapping

For high-resolution images of the samples a JEM-2200FS (JEOL) TEM operating at 200 kV was used. EDX mapping was performed in STEM mode using an Oxford X-Max 100 TLE detector.

3.5.6 | Temperature Programmed Reduction (TPR)

Temperature programmed reduction using H_2 was measured using a ChemBET Pulsar (Fa. Quantachrome Instruments). Prior to the experiment, the samples (0.05 g) were exposed to a N_2 gas flow (80 NmL/min) and heated up to 200°C (20°C/min) for 10 min to remove surface H_2O, followed by cooling down to 40°C. The sample was heated up again under H_2/N_2 (5/95 v/v) gas flow (80 NmL/min, 30°C/min) to 850°C. The H_2 uptake was measured by a thermal conductivity detector (TCD).

3.5.7 | N_2-Physisorption

Low temperature N_2 adsorption–desorption analysis was used (Nova 3000e Surface Area Analyzer, Quantachrome Instruments) to determine the mass specific surface area (S_m), mesopore size distribution, and mesopore volume (V_{meso}) of the catalysts. An overall sample mass of ≈20 mg was used for each analysis. Samples were degassed under vacuum at a temperature of 100°C for 6 h prior to analysis. *S*m was estimated using the BET (Brunauer–Emmett–Teller) method based on highly correlated linear fitting of the BET model (p/p_0 range = 0.027–0.27, $R2 \geq 0.9998$) derived from Type IV N_2 adsorption isotherms. V_{meso} and the mean mesopore diameter ($d_{pore,\ mean}$) were estimated via the BJH (Barrett–Joyner–Halenda) method.

3.6 | Analytics for Experimental Evaluation

3.6.1 | High Performance Liquid Chromatography (HPLC)

The liquid phase collected after the reaction was analyzed by high-performance liquid chromatography (HPLC) for various products. For this purpose, each sample has been filtered (0.45 µm) prior to analysis. The used HPLC is a Nexera 40 from SHIMADZU with a polymer phase organic acid column, 300 m x 8 mm from the company Chromatographie-Service GmbH. The eluent used was a sulphuric acid solution with a concentration of 4 mmol/L at a flow rate of 0.8 mL/min at 25°C. The detection sensor after the column is a refractive index detector (RID). The detected products were calibrated. A sample chromatogram containing all possible compounds of the reaction is shown in Figure S18, whereby Table S4 shows the measured retention

times. Figure S19 shows the calibration curves of the detected compounds.

3.6.2 | Gas Chromatography (GC)

The gas samples were analyzed with a Varian 450-GC equipped with a Shin-Carbon-ST-Column of 2 m × 0.75 mm. The samples were injected through a 250 µL sample tube and were passed through the column in a stationary phase. The temperature program includes an initial temperature of 40°C, for 2.5 min. After that column is heated to 250°C in 11.5 min. This temperature is kept for an additional 12 min. The front column pressure was set to 70 psi, the one in the middle to 10 psi. The products were analyzed with a Thermal Conductivity Detector (TCD) with a setpoint of 300°C and a Flame Ionization Detector (FID) that is set to 200°C. The detectable products have been calibrated. Example chromatograms of the TCD and FID are shown in Figures S20 and S21.

3.6.3 | Nuclear Magnetic Resonance Spectroscopy (NMR)

The liquid samples have been analyzed qualitatively by using ^{1}H and ^{13}C NMR. All NMR spectra were measured with a Bruker AVANCEII at 600 MHz. The samples were prepared as follows: 600 µL of the filtered reaction solution and 100 µL D_2O as a deuterated solvent were filled in an NMR tube. The NMR analysis was done with the software MestReNova.

4 | Conclusions

This study showed a rigorous catalyst optimization study for an efficient CNT-supported glycerol hydrogenolysis catalyst. This included the synthesis and characterization of several mono-, bi-, and trimetallic catalysts for the hydrogenolysis of glycerol to 1,2-propanediol. Combining the activity of Ru with the selectivity of Cu and supporting them on commercial NC7000 carbon nanotubes using a simple wetness impregnation method resulted in a highly dispersed catalyst that showed a 58% yield of 1,2-PDO at 220°C with a high selectivity for the desired product of 81%. Motivated by a statistical modeling approach, the ratio between the two most promising metals, Ru and Cu, was further optimized. The experimental results prove the benefits of the bimetallic catalyst, and the model-based analysis indicates further potential for improvement. To advance toward a data-driven catalyst design, a systematic experimental campaign guided by DoE is recommended, targeting intermediate compositions and catalyst masses where the current model uncertainty is highest.

Acknowledgments

This project is funded by the Deutsche Forschungsgemeinschaft (DFG, German Research Foundation) SFB 1615 –503850735. We kindly acknowledge Bo Elfers and his team of the central analytics of TUHH for performing the ICP-OES measurements, Isabelle Nevoigt for carrying out the XRD measurements, as well as Stephan Bartling (LiKAT) for performing and analyzing the XPS samples. Many thanks to Philipp Kampe, Nick Herrmann, Jan-Dominik Krueger, and Daniel Niehaus for participating in many helpful discussions for the project. A special thanks to Ira Wirth for her help in carrying out some of the experiments during her research internship.

Open access funding enabled and organized by Projekt DEAL.

Conflicts of Interest

The authors have no conflicts of interest.

Data Availability Statement

Research data is available after official publication (https://doi.org/10.15480/882.16291).

References

1. National Reasearch Council, *Adapting to the Impacts of Climate Change*; (The National Academies Press, 2010), https://doi.org/10.17226/12783.

2. A. Behr and T. Seidensticker, Das Koppelprodukt Der Oleochemie. In *Einführung in die Chemie Nachwachsender Rohstoffe: Vorkommen, Konversion, Verwendung*; (Springer, 2018), https://doi.org/10.1007/978-3-662-55255-1_5.

3. S. Pinzi, I. L. Garcia, F. J. Lopez-Gimenez, M. D. Luque de Castro, G. Dorado, and M. P. Dorado, "The Ideal Vegetable Oil-Based Biodiesel Composition: A Review of Social, Economical and Technical Implications", *Energy & Fuels* 23, no. 5 (2009): 2325–2341, https://doi.org/10.1021/ef801098a.

4. M. Checa, S. Nogales-Delgado, V. Montes, and J. M. Encinar, "Recent Advances in Glycerol Catalytic Valorization: A Review", *Catalysts* 10 (2020): 1279, https://doi.org/10.3390/catal10111279.

5. A. Modvig, C. Kumpidet, A. Riisager, and J. Albert, "Ru-Doped Wells–Dawson Polyoxometalate as Efficient Catalyst for Glycerol Hydrogenolysis to Propanediols", *Materials* 12 (2019): 2175, https://doi.org/10.3390/ma12132175.

6. Y. Wang, J. Zhou, and X. Guo, "Catalytic Hydrogenolysis of Glycerol to Propanediols: A Review", *RSC Advances* 5, no. 91 (2015): 74611–74628, https://doi.org/10.1039/C5RA11957J.

7. I. C. Wirth, D. Niehaus, D. Voß, M. Schlüter, and J. Albert, "Advanced Glycerol Oxidation to Formic Acid in a Multiphasic Jet Loop Reactor Using Polyoxometalate Catalysts", *ACS Sustainable Chemistry & Engineering* 14, no. 1 (2025): 551–565, https://doi.org/10.1021/acssuschemeng.5c10177.

8. M. A. Dasari, P. P. Kiatsimkul, W. R. Sutterlin, and G. J. Suppes, "Low-Pressure Hydrogenolysis of Glycerol to Propylene Glycol", *Applied Catalysis A: General* 281, no. 1–2 (2005): 225–231, https://doi.org/10.1016/j.apcata.2004.11.033.

9. M. N. Gatti, F. M. Perez, G. F. Santori, and F. Pompeo, "Mechanism Analysis and Chemical Equilibrium Modelling for Liquid Phase Glycerol Hydrogenolysis", *Chemical Thermodynamics and Thermal Analysis* 18 (2025): 100186, https://doi.org/10.1016/j.ctta.2025.100186.

10. D. Coll, F. Delbecq, Y. Aray, and P. Sautet, "Stability of Intermediates in the Glycerol Hydrogenolysis on Transition Metal Catalysts From First Principles", *Physical Chemistry Chemical Physics* 13, no. 4 (2011): 1448–1456, https://doi.org/10.1039/C0CP00858C.

11. L. Ma, H. Liu, and D. He, "Recent Progress in Catalyst Development of the Hydrogenolysis of Biomass-Based Glycerol Into Propanediols—A Review", *Bioengineering* 10, no. 11 (2023): 1264, https://doi.org/10.3390/bioengineering10111264.

12. P. Koranian, Q. Huang, A. K. Dalai, and R. Sammynaiken, "Chemicals Production From Glycerol Through Heterogeneous Catalysis: a Review", *Catalysts* 12, no. 8 (2022): 897, https://doi.org/10.3390/catal12080897.

13. S. Wang, K. Yin, Y. Zhang, and H. Liu, "Glycerol Hydrogenolysis to Propylene Glycol and Ethylene Glycol on Zirconia Supported Noble

Metal Catalysts", *ACS Catalysis* 3 (2013): 2112–2121, https://doi.org/10.1021/cs400486z.

14. C. Montassier, D. Giraud, and J. Barbier, "Polyol Conversion by Liquid Phase Heterogeneous Catalysis over Metals", *Heterogeneous Catalysis and Fine Chemicals*, Eds. M. Guisnet, J. Barrault, C. Bouchoule, D. Duprez, C. Montassier, G. Pérot, (Elsevier, 1988), https://doi.org/10.1016/S0167-2991(09)60811-9.

15. E. P. Maris and R. J. Davis, "Hydrogenolysis of Glycerol Over Carbon-Supported Ru and Pt Catalysts", *Journal of Catalysis* 249, no. 2 (2007): 328–337, https://doi.org/10.1016/j.jcat.2007.05.008.

16. J. Albert, A. Bukowski, and J. Krueger, "Liquid phase process for preparing acrylic acid from glycerol", Patent WO 2024156344A1, 2023.

17. Z. Wu, Y. Mao, X. Wang, and M. Zhang, "Preparation of a Cu–Ru/Carbon Nanotube Catalyst for Hydrogenolysis of Glycerol to 1,2-propanediol via Hydrogen Spillover", *Green Chemistry* 13, no. 5 (2011): 1311, https://doi.org/10.1039/c0gc00809e.

18. Y. Nakagawa and K. Tomishige, "Heterogeneous Catalysis of the Glycerol Hydrogenolysis", *Catalysis Science & Technology* 1, no. 2 (2011): 179, https://doi.org/10.1039/C0CY00054J.

19. A. Żelazny, K. Samson, R. Grabowski, M. Śliwa, M. Ruggiero-Mikołajczyk, and A. Kornas, "Hydrogenolysis of Glycerol to Propylene Glycol Over Cu/Oxide Catalysts: Influence of the Support and Reaction Conditions", *Reaction, Kinetics, Mechanisms and Catalysis* 121, no. 1 (2017): 329–343, https://doi.org/10.1007/s11144-017-1154-6.

20. S. M. Pudi, P. Biswas, and S. Kumar, "Selective Hydrogenolysis of Glycerol to 1,2-propanediol Over Highly Active Copper–Magnesia Catalysts: Reaction Parameter, Catalyst Stability and Mechanism Study", *Journal of Chemical Technology & Biotechnology* 91, no. 7 (2016): 2063–2075, https://doi.org/10.1002/jctb.4802.

21. K.-T. Li, C.-H. Wang, and H.-C. Wang, "Hydrogenolysis of Glycerol to 1,2-propanediol on Copper Core-Porous Silica Shell-Nanoparticles", *Journal of the Taiwan Institute of Chemical Engineers* 52 (2015): 79–84, https://doi.org/10.1016/j.jtice.2015.02.011.

22. J. Zhao, W. Yu, C. Chen, H. Miao, H. Ma, and J. Xu, "Ni/NaX: A Bifunctional Efficient Catalyst for Selective Hydrogenolysis of Glycerol", *Catalysis Letters* 134, no. 1 (2010): 184–189, https://doi.org/10.1007/s10562-009-0208-4.

23. A. Marinoiu, G. Ionita, C.-L. Gáspár, C. Cobzaru, and S. Oprea, "Glycerol Hydrogenolysis to Propylene", *Reaction Kinetics and Catalysis Letters* 97, no. 2 (2009): 315–320, https://doi.org/10.1007/s11144-009-0032-2.

24. A. V.-H. Soares, G. Perez, and F. B. Passos, "Alumina Supported Bimetallic Pt–Fe Catalysts Applied to Glycerol Hydrogenolysis and Aqueous Phase Reforming", *Applied Catalysis B: Environmental* 185 (2016): 77–87, https://doi.org/10.1016/j.apcatb.2015.11.003.

25. T. Miyazawa, Y. Kusunoki, K. Kunimori, and K. Tomishige, "Glycerol Conversion in the Aqueous Solution Under Hydrogen Over Ru/C + an Ion-Exchange Resin and Its Reaction Mechanism", *Journal of Catalysis* 240, no. 2 (2006): 213–221, https://doi.org/10.1016/j.jcat.2006.03.023.

26. B. Li, J. Wang, Y. Yuan, H. Ariga, S. Takakusagi, and K. Asakura, "Carbon Nanotube-Supported RuFe Bimetallic Nanoparticles as Efficient and Robust Catalysts for Aqueous-Phase Selective Hydrogenolysis of Glycerol to Glycols", *ACS Catalysis* 1, no. 11 (2011): 1521–1528, https://doi.org/10.1021/cs200386q.

27. H. Liu, S. Liang, T. Jiang, B. Han, and Y. Zhou, "Hydrogenolysis of Glycerol to 1,2-Propanediol Over Ru–Cu Bimetals Supported on Different Supports", *CLEAN—Soil, Air, Water* 40, no. 3 (2012): 318–324, https://doi.org/10.1002/clen.201000227.

28. M. Sherbi, A. Wesner, V. K. Wisniewski, et al., "Superior CNT-Supported Bimetallic RuCu Catalyst for the Highly Selective Hydrogenolysis of Glycerol to 1,2-Propanediol", *Catalysis Science & Technology* 11 (2021): 6649–6653, https://doi.org/10.1039/d1cy01518d.

29. A. Wesner, M. P. Papajewski, L. Schidowski, C. Ruhmlieb, M. J. Poller, and J. Albert, "Supported $H_8PV_5Mo7O_{40}$ on Activated Carbon: Synthesis and Investigation of Influencing Factors for Catalytic Performance", *Dalton Transactions* 53 (2024): 14065–14076, https://doi.org/10.1039/D4DT01336K.

30. R. Xu, L. Yang, H. Fang, et al., "Cu Complexes in Carbon Nanotubes as Catalysts for Thermal Decomposition of Energetic Oxidizers," *ACS Applied Nano Materials Journal* 5, no. 10 (2022): 14942–14953, https://doi.org/10.1021/acsanm.2c03191.

31. X. Zhao, J. Wang, M. Yang, et al., "Selective Hydrogenolysis of Glycerol to 1,3-Propanediol: Manipulating the Frustrated Lewis Pairs by Introducing Gold to Pt/WO x," *Chemsuschem* 10, no. 5 (2017): 819–824, https://doi.org/10.1002/cssc.201601503.

32. M. Sherbi, M. Stuckart, and J. Albert, "Selective Catalytic Hydrogenation of Biomass Derived Furans to Secondary Alcohols Using Pt/Polyoxometalate Catalysts Under Mild Reaction Conditions," *Biofuels, Bioproducts and Biorefining* 15, no. 5 (2021): 1431–1446, https://doi.org/10.1002/bbb.2248.

Supporting Information

Additional supporting information can be found online in the Supporting Information section.

Supporting File: cctc70642-sup-0001-SuppMat.docx.